Available online at www.sciencedirect.com
ScienceDirect
International Journal of Heat and Mass Transfer 51 (2008) 2566–2582
International Journal of HEAT and MASS TRANSFER
www.elsevier.com/locate/ijhmt

Numerical simulation of nucleate boiling on a horizontal surface at high heat fluxes

Gihun Son [a,*], Vijay K. Dhir [b]

[a] Department of Mechanical Engineering, Sogang University, Seoul 121-742, South Korea
[b] Mechanical and Aerospace Engineering Department, University of California, Los Angeles, CA 90095, USA

Received 12 April 2007; received in revised form 24 July 2007
Available online 29 September 2007

Abstract

Nucleate boiling at high heat fluxes has been studied numerically by solving the equations governing conservation of mass, momentum and energy in the liquid and vapor phases. The interface is captured by using the level set method based on a sharp-interface representation. The evaporative heat flux from the liquid microlayer is incorporated in the analysis. The effects of wall superheat, number density of nucleation sites and waiting period on the bubble dynamics and heat transfer in nucleate boiling are investigated. The heat fluxes obtained from the present numerical simulations are compared with the experimental data reported in the literature.

Keywords: Nucleate boiling; Level set method; Numerical simulation

1. Introduction

In nucleate boiling, vapor bubbles form at discrete sites on a heated surface. The frequency of bubble release and the number density of active nucleation sites increase with wall superheat or heat flux. At high wall superheats, the bubbles merge in the vertical and lateral directions, which leads to formation of vapor columns and mushroom type bubbles, as observed by Gaertner [1]. The mushroom type bubbles are supported by vapor stems connecting the vapor mass to the heater surface. As the boiling process is one of the most efficient modes of heat transfer, it has been studied extensively over the last several decades. A number of empirical and mechanism-based correlations for nucleate boiling have been reported in the literature, as reviewed in detail by Dhir [2,3]. However, because of the complexity of the process involving vapor–liquid interfaces that evolve, merge and break up in time, the flow and temperature fields influenced by the interfacial motion, and the microlayer that forms between the solid and the vapor phase near the wall, a general predictive model for nucleate boiling has not yet been developed.

Recently, numerical simulations for directly analyzing the bubble dynamics and heat transfer in nucleate boiling have been performed by several investigators. Lee and Nydahl [4] computed the bubble growth in nucleate boiling by using a numerical mapping method to solve the mass, momentum and energy equations. In their analysis, the bubble was assumed to remain hemispherical in shape during its growth. To obtain the bubble shape as part of the solution, Welch [5] carried out more generalized computations based on an unstructured moving-grid method. However, his method was not extended for configurations with large interfacial distortion or change in topology such as observed during bubble departure. Son et al. [6] performed a complete numerical simulation of a growing and departing bubble during partial nucleate boiling by employing the level set (LS) method, which can handle the bubble departure process. They included the effect of microlayer evaporation in the analysis as well. The LS method was also applied to simulation of bubble merger in the vertical direction at a single nucleation site [7]. Subsequently, Mukherjee

* Corresponding author. Tel.: +82 2 705 8641; fax: +82 2 712 0799.
E-mail address: gihun@sogang.ac.kr (G. Son).

0017-9310/$ - see front matter © 2007 Elsevier Ltd. All rights reserved.
doi:10.1016/j.ijheatmasstransfer.2007.07.046

Nomenclature

A	dispersion constant
c	specific heat
F	fraction function
g	gravity
h	grid spacing
h_{lv}	latent heat of vaporization
H	discontinuous step function
k	thermal conductivity
l_o	reference length, $\sqrt{\sigma/g(\rho_l-\rho_v)}$
$\dot{m}$	mass flux across the interface
$\mathbf{n}$	unit normal vector
N	number density of active nucleation sites
Nu	Nusselt number, $ql_o/k_l\Delta T$
p	pressure
Pr	Prandtl number, $\mu c/k$
q	heat flux
R_v	gas constant
s	spacing between the active sites
S	sign function
t	time
t_o	reference time, $\sqrt{l_o/g}$
T	temperature
ΔT	temperature difference, $T_w - T_{sat}$
$\mathbf{u}$	velocity vector
$\mathbf{U}$	interface velocity vector
v_{vl}	$\rho_v^{-1}-\rho_l^{-1}$
X_o	x-directional location of dry region beneath a bubble
X_l	x-directional location of the interface at $y = h/2$
x, y	Cartesian coordinates

Greek symbols

α	thermal diffusivity
β_T	coefficient of thermal expansion
δ	liquid film thickness
δ_o	non-evaporating liquid film thickness
κ	interface curvature
μ	dynamic viscosity
ρ	density
σ	surface tension coefficient
τ	artificial time
τ_w	waiting period
ϕ	level set function
φ	contact angle

Subscripts

f	liquid or vapor
int	interface
l, v	liquid, vapor
sat, w	saturation, wall

and Dhir [8] further extended the LS method for three-dimensional computations of lateral merger of bubbles nucleating at two and three neighboring sites. Shin et al. [9] also performed a three-dimensional numerical simulation of nucleate boiling by using the level contour reconstruction method, which is a simplified front tracking method. To account for the effect of active site density on nucleate boiling heat flux, the numerical simulation was made for a single bubble on an effective surface area corresponding to the number density of active sites on a real surface.

The past numerical simulations have been limited to nucleate boiling at relatively low heat fluxes, in which the vertical and horizontal interactions between bubbles are not so complex. The objective of this study is to perform numerical simulations of nucleate boiling at high wall superheats and to investigate the effects of wall superheat, number density of active nucleation sites and waiting period on the bubble dynamics and wall heat transfer. As a preliminary attempt to predict nucleate boiling heat flux on a commercial surface at high superheats, numerical simulations are carried out under the assumption that the boiling process is two-dimensional. In reality nucleate boiling at high superheats including the lateral merger of bubbles is three-dimensional. However, the numerical simulation for such three-dimensional characteristics of the process requires a tremendous computational time and only a comparison between 3D and 2D results is made here for one single case.

2. Numerical analysis

Fig. 1 shows the configuration used in this study for simulation of nucleate boiling on a horizontal surface. A liquid microlayer, which forms between the bubble and the wall near the bubble-wall contact location, has a thickness varying from the mesh size to the order of the size of a few mol-

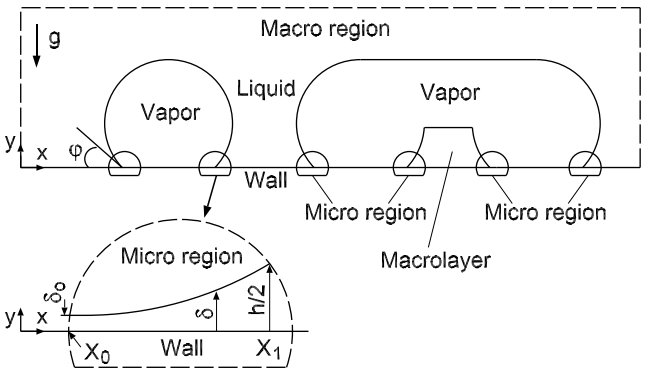

Fig. 1. Macro and micro regions used in numerical simulation.

ecules. As such, the computational domain is divided into a liquid microlayer (or micro region) and the vapor–liquid (or macro) region excluding microlayer, as was used in the work of Son et al. [6]. The results of microlayer analysis are incorporated into numerical simulation for the macro region. In carrying out the analysis flows are taken to be laminar. The fluid properties including density, viscosity and thermal conductivity are assumed to be constant in each phase.

The conservation equations of mass, momentum and energy in the microlayer are derived by using a lubrication theory [10,11] as

$$\frac{\partial}{\partial x}\int_o^\delta \rho_l u_l \,\mathrm{d}y = -\frac{q}{h_{lv}} \tag{1}$$

$$\frac{\partial p_l}{\partial x} = \mu_l \frac{\partial^2 u_l}{\partial y^2} \tag{2}$$

$$q = k_l \frac{T_w - T_{int}}{\delta} \tag{3}$$

Using a modified Clausius–Clayperon equation, the evaporative heat flux is written as

$$q = h_{ev}[T_{int} - T_v + (p_l - p_v)T_v/\rho_l h_{lv}] \tag{4}$$

where

$$h_{ev} = (2/\pi R_v T_v)^{0.5}\rho_v h_{lv}^2/T_v; \quad T_v = T_{sat}(p_v) \tag{5}$$

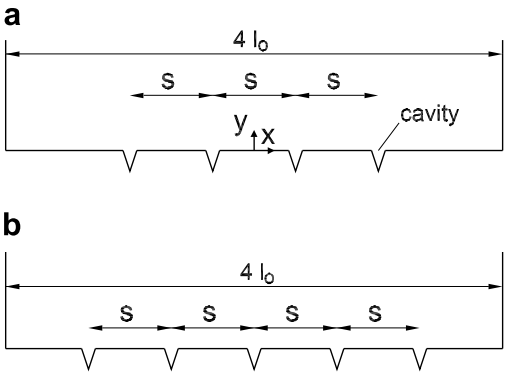

Fig. 2. Configuration of active nucleation sites: (a) $N = 4/4$ and (b) $N = 5/4$.

The pressures in the vapor and liquid phases are related as

$$p_l = p_v - \sigma\kappa - \frac{A}{\delta^3} + \frac{q^2}{\rho_v h_{lv}^2} \tag{6}$$

where σ is taken to be a function of temperature and A is the dispersion constant relating disjoining pressure to the film thickness. The combination of the mass, momentum, and energy equations for the microlayer yields

$$\delta'''' = f(\delta, \delta'\delta''\delta''') \tag{7}$$

where $'$ denotes $\partial/\partial x$. The boundary conditions for the above equation are as follows: at $x = X_o$,

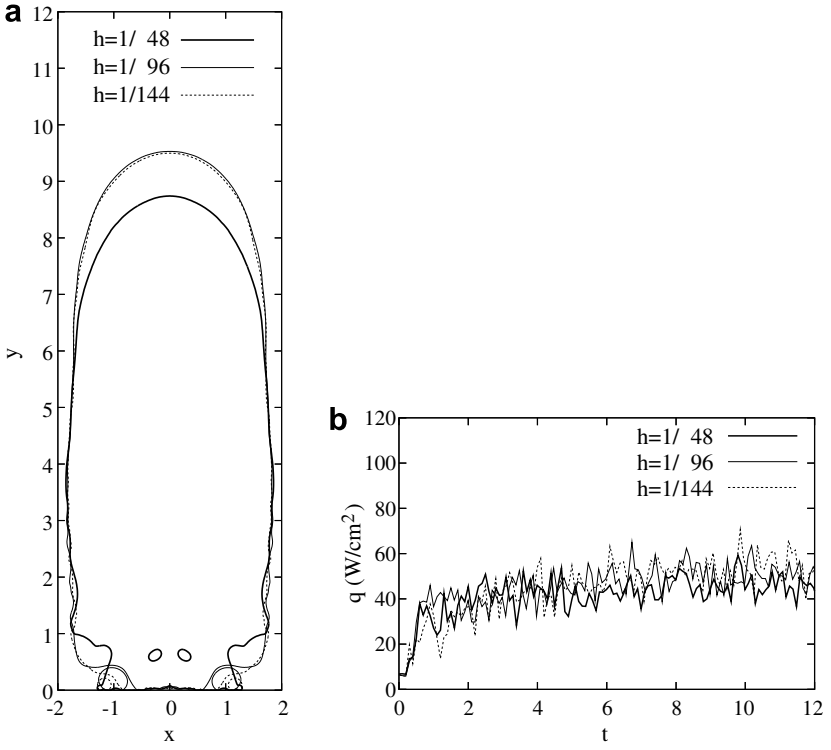

Fig. 3. Effect of mesh size on the numerical results for $\Delta T_w = 25$ °C, $N = 11/4$, $s = 0.25$, and $\tau_w = 0.1$: (a) the liquid–vapor interface shape at $t = 5.5$ and (b) the wall heat flux averaged over the heater area.

$$\delta = \delta_o; \quad \delta' = \delta''' = 0 \tag{8}$$

at $x = X_1$,

$$\delta = h/2; \quad \delta' = \tan\varphi; \quad \delta'' = 0 \tag{9}$$

where δ_o is of the order of molecular size [11], $h/2$ is the distance to the first computational node from the wall for the level set function, ϕ, and φ is an apparent contact angle that is measurable experimentally. In implementing the above boundary conditions the location X_1 is determined from the solution of macro region. For a given contact angle, the microlayer formulation, Eq. (7), is integrated using six boundary conditions, Eqs. (8) and (9), under the condition that the dispersion constant and X_o are unknown.

For numerically analyzing the macro region, the sharp-interface level set (LS) formulation modified by Son and Dhir [12] to include the effect of phase-change at the liquid–vapor interface is used. The liquid–vapor interface is tracked by a LS function, ϕ, which is defined as a signed distance from the interface. The negative sign is chosen for

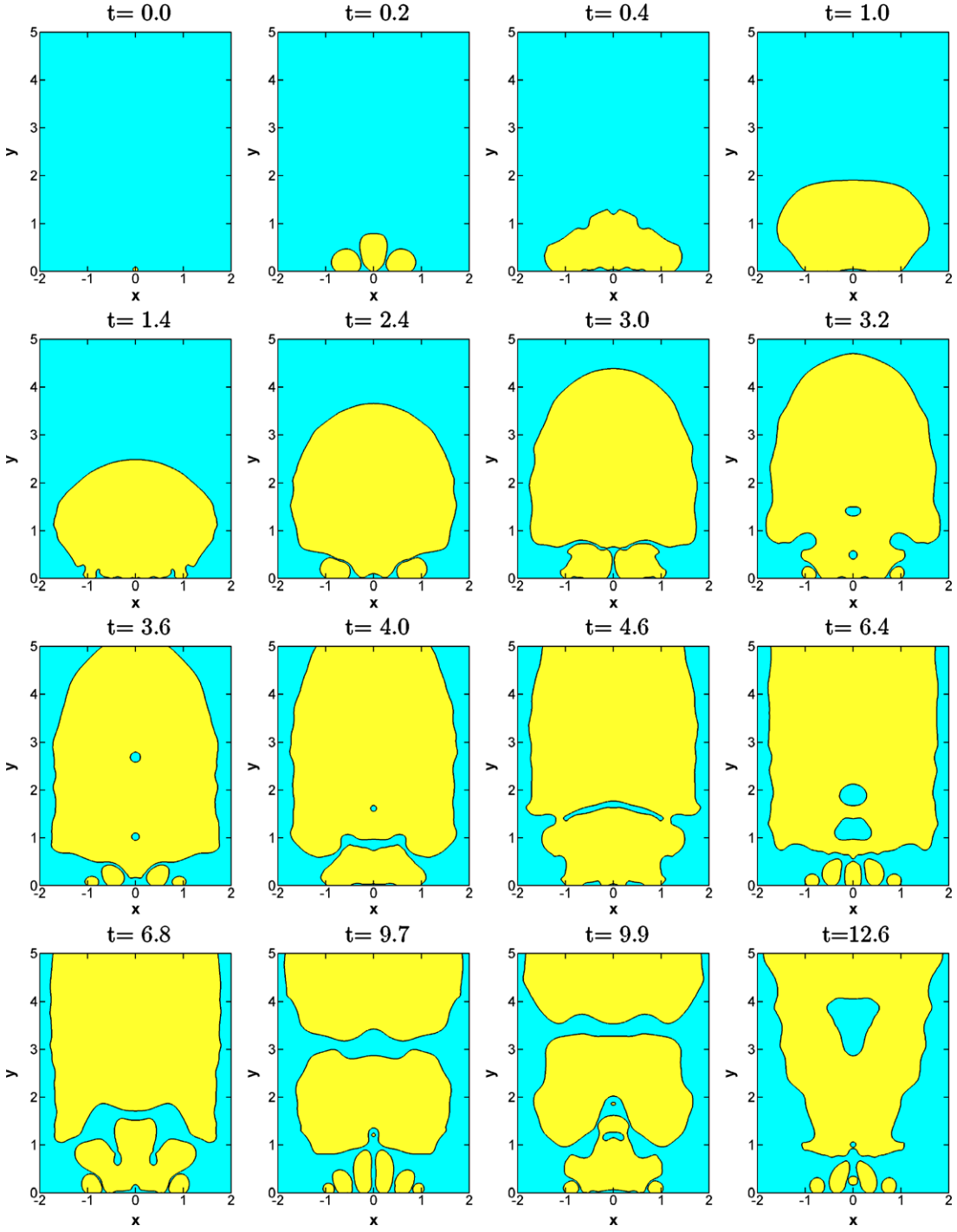

Fig. 4. Bubble growth and merger for $\Delta T = 25$ °C, $N = 5/4$, $s = 0.5$, and $\tau_w = 0.1$.

the vapor phase and the positive sign for the liquid phase. Considering that the heat flux through the vapor phase is much smaller than that through the liquid phase, we assume that the vapor phase is maintained at the saturation temperature.

The equations governing the conservation of mass, momentum and energy for each phase are written as

$$\nabla \cdot \mathbf{u}_f = 0 \tag{10}$$

$$\rho_f\left(\frac{\partial \mathbf{u}_f}{\partial t} + \mathbf{u}_f \cdot \nabla \mathbf{u}_f\right) = -(\nabla p)_f + \rho_f[1 - \beta_T(T_f - T_{sat})]\mathbf{g} + \nabla \cdot \mu_f(\nabla \mathbf{u} + \nabla \mathbf{u}^T)_f \tag{11}$$

$$\rho_f c_f\left(\frac{\partial T_f}{\partial t} + \mathbf{u}_f \cdot \nabla T_f\right) = \nabla \cdot k_f(\nabla T)_f \tag{12}$$

where the subscript "f" denotes the liquid phase for $\phi > 0$ and the vapor phase for $\phi < 0$. The conservation equations for each phase are coupled through the matching (or jump) conditions at the interface:

$$\mathbf{u}_l - \mathbf{u}_v = v_{lv}\dot{m}\mathbf{n} \tag{13}$$

$$\mathbf{n} \cdot \left[\mu_l(\nabla \mathbf{u} + \nabla \mathbf{u}^T)_l - \mu_v(\nabla \mathbf{u} + \nabla \mathbf{u}^T)_v\right] \times \mathbf{n} = 0 \tag{14}$$

$$-p_l + p_v + \mathbf{n} \cdot \left[\mu_l(\nabla \mathbf{u} + \nabla \mathbf{u}^T)_l - \mu_v(\nabla \mathbf{u} + \nabla \mathbf{u}^T)_v\right] \cdot \mathbf{n} = \sigma\kappa - v_{lv}\dot{m}^2 \tag{15}$$

where $v_{lv} = \rho_v^{-1} - \rho_l^{-1}$. The normal, $\mathbf{n}$, to the interface, the interface curvature, κ, and the mass flux, $\dot{m}$, are defined as

$$\mathbf{n} = \nabla\phi/|\nabla\phi| \tag{16}$$

$$\kappa = \nabla \cdot \mathbf{n} \tag{17}$$

$$\dot{m} = \rho_f(\mathbf{U} - \mathbf{u}_f) \cdot \mathbf{n} \tag{18}$$

where $\mathbf{U}$ is the interface velocity. The interface temperature is specified as a Dirichlet boundary condition, $T_f = T_{sat}$. The mass flux $\dot{m}$ is evaluated from the energy balance at the interface

$$\dot{m} = \mathbf{n} \cdot k_l \nabla T_l / h_{lv} \tag{19}$$

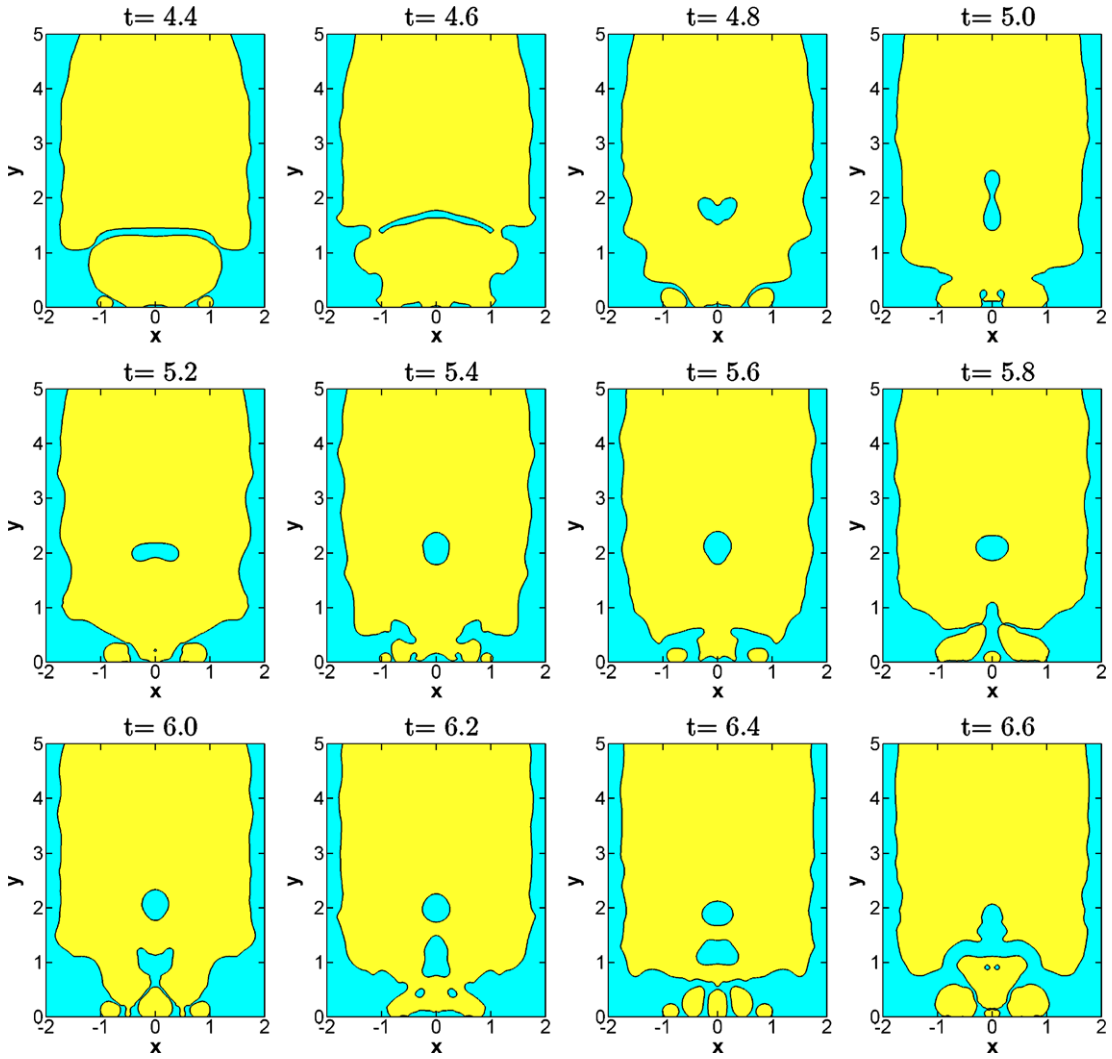

Fig. 5. Behavior of liquid droplets entrapped during bubble growth and merger for $\Delta T = 25$ °C, $N = 5/4$, $s = 0.5$, and $\tau_w = 0.1$.

For its efficient implementation, $\dot{m}$ is extrapolated into the entire domain (or a narrow band near the interface) by the calculation procedure developed in [13].

Based on the ghost fluid approach [13–19], which is a numerical technique for accurately enforcing the boundary or matching conditions at the interface without being smoothed over several grid spacings, the conservation equations can be rewritten for the liquid–vapor region as

$$\nabla \cdot \mathbf{u} = v_{\mathrm{lv}} \dot{m} \mathbf{n} \cdot \nabla H + \dot{V}_{\mathrm{micro}} \tag{20}$$

$$\hat{\rho}\left(\frac{\partial \mathbf{u}}{\partial t} + \mathbf{u}_{\mathrm{f}} \cdot \nabla \mathbf{u}_{\mathrm{f}}\right) = -[\nabla p + (\sigma\kappa - v_{\mathrm{lv}}\dot{m}^2)\nabla H] + \hat{\rho}[1 - \beta_{\mathrm{T}}(T_{\mathrm{f}} - T_{\mathrm{sat}})]\mathbf{g} + \nabla \cdot \hat{\mu}[\nabla \mathbf{u} - v_{\mathrm{lv}}\dot{m}\mathbf{n}\nabla H + (\nabla \mathbf{u} - v_{\mathrm{lv}}\dot{m}\mathbf{n}\nabla H)^{\mathrm{T}}] \tag{21}$$

$$\rho_{\mathrm{f}} c_{\mathrm{f}}\left(\frac{\partial T_{\mathrm{f}}}{\partial t} + \mathbf{u}_{\mathrm{f}} \cdot \nabla T_{\mathrm{f}}\right) = \nabla \cdot \hat{k}_{\mathrm{f}} \nabla T_{\mathrm{f}} \quad \text{if} \quad \phi > 0$$

$$T_{\mathrm{f}} = T_{\mathrm{sat}} \quad \text{if} \quad \phi \leqslant 0 \tag{22}$$

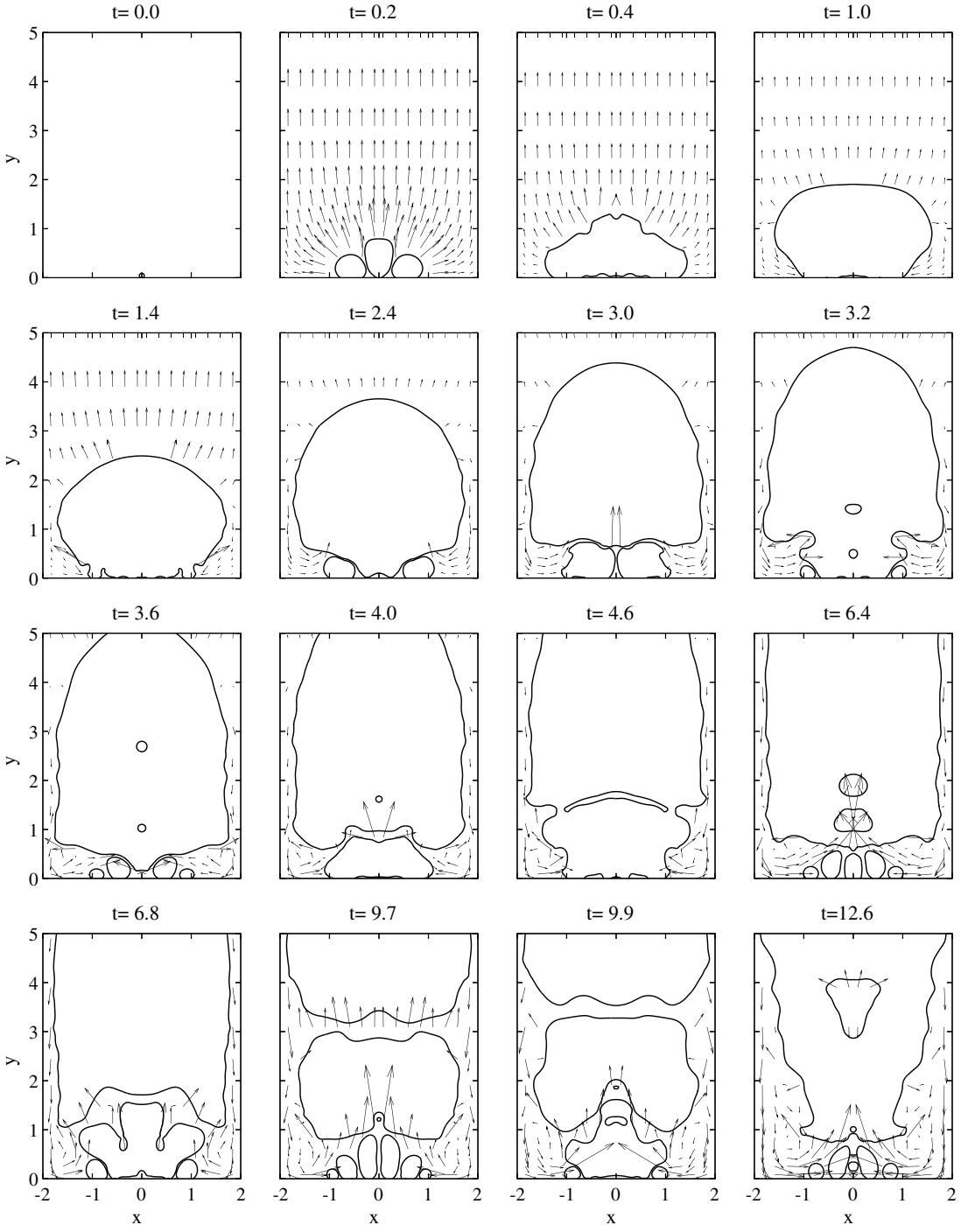

Fig. 6. Liquid velocity field for $\Delta T = 25$ °C, $N = 5/4$, $s = 0.5$, and $\tau_{\mathrm{w}} = 0.1$.

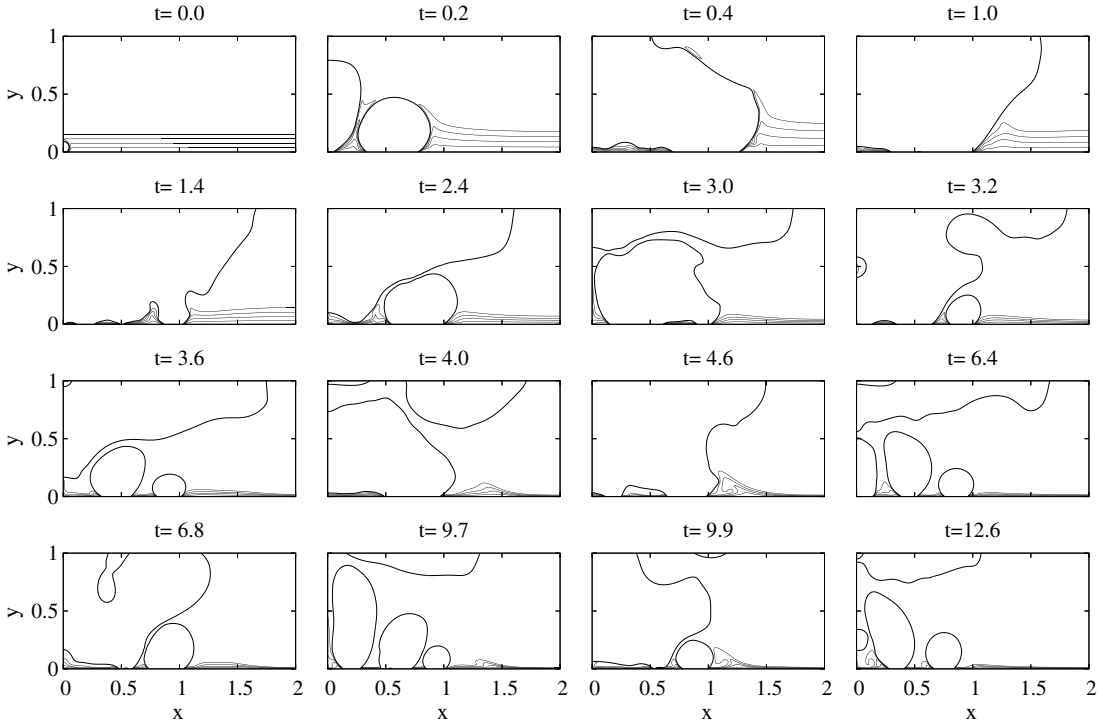

Fig. 7. Temperature field for $\Delta T = 25\ ^\circ\mathrm{C}$, $N = 5/4$, $s = 0.5$, and $\tau_w = 0.1$.

where

$$
\begin{aligned}
&H = 1 \quad \text{if} \quad \phi > 0 \\
&\quad = 0 \quad \text{if} \quad \phi \leqslant 0 \\
&\mathbf{u}_l = \mathbf{u} + v_{lv}\dot{m}\mathbf{n}(1-H) \\
&\mathbf{u}_v = \mathbf{u} - v_{lv}\dot{m}\mathbf{n}H \\
&\hat{\rho} = \rho_v(1-F) + \rho_l F \\
&\hat{\mu}^{-1} = \mu_v^{-1}(1-F) + \mu_l^{-1}F \\
&\hat{k}_f = \hat{k}_l = k_l/F
\end{aligned}
$$

Here, H is the discontinuous step function rather than the smoothed step function varying over several grid spacings and $\mathbf{u}_f$ ($\mathbf{u}_l$ or $\mathbf{u}_v$) is the velocity for each phase which is extrapolated into the entire domain by using the velocity jump condition given by Eq. (13). The effective (or interpolated) properties, ($\hat{\rho}$, $\hat{\mu}$, and $\hat{k}_f$), are evaluated from a fraction function, F, which is defined as

$$
\begin{aligned}
F &= 1 \quad \text{if} \quad H(\phi_A) = H(\phi_B) = 1 \\
&= 0 \quad \text{if} \quad H(\phi_A) = H(\phi_B) = 0 \\
&= \frac{\max(\phi_A, \phi_B)}{\max(\phi_A, \phi_B) - \min(\phi_A, \phi_B)} \quad \text{otherwise}
\end{aligned}
$$

where ϕ_A and ϕ_B are obtained at the adjacent grid points [12]. In Eq. (20), $\dot{V}_{\text{micro}}$ is obtained from the microlayer solution as

$$
\dot{V}_{\text{micro}} = \int_{X_o}^{X_1} \frac{k_l(T_w - T_{\text{int}})}{\rho_v h_{lv} \delta \Delta V_{\text{micro}}}\, \mathrm{d}x \tag{23}
$$

where ΔV_{micro} is a vapor-side control volume near the micro region.

In the LS formulation, the interface is described as $\phi = 0$. The zero level set of ϕ is advanced as

$$
\frac{\partial \phi}{\partial t} + \mathbf{U} \cdot \nabla \phi = 0 \tag{24}
$$

where $\mathbf{U}$ can be written from Eq. (18) as $\mathbf{U} = \mathbf{u}_f + \dot{m}\mathbf{n}/\rho_f$. The LS function is reinitialized to a distance function from the interface by obtaining a steady-state solution of the equation

$$
\frac{\partial \phi}{\partial \tau} = S(\phi_o)(1 - |\nabla \phi|) \tag{25}
$$

where

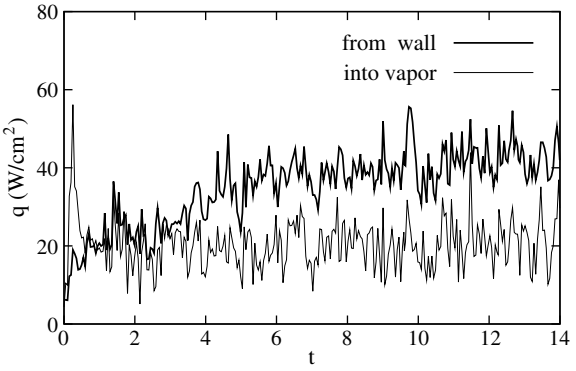

Fig. 8. Temporal variation of heat fluxes from wall and into vapor for $\Delta T = 25\ ^\circ\mathrm{C}$, $N = 5/4$, $s = 0.5$, and $\tau_w = 0.1$.

$$S(\phi_o) = 0 \quad \text{if } |\phi_o| \leqslant d_\epsilon$$
$$= \frac{\phi_o}{\sqrt{\phi_o^2 + h^2}} \quad \text{otherwise} \tag{26}$$

Here h is a grid spacing, ϕ_o is a solution of Eq. (24), and d_ϵ is the distance between the interface and the nearest grid point. The formulation given by Eq. (26) implies that a near-zero level set rather than $\phi = 0$ is used as the immobile boundary condition during the reinitialization procedure. This formulation of the sign function improves the LS method significantly [20].

To preserve mass conservation from any numerical errors occurring in numerical implementation of the LS advection and reinitialization procedures, the following volume-correction step is added to the level set formulation:

$$\frac{\partial \phi}{\partial \tau} = (V_v - V_{v0})|\nabla \phi| \tag{27}$$

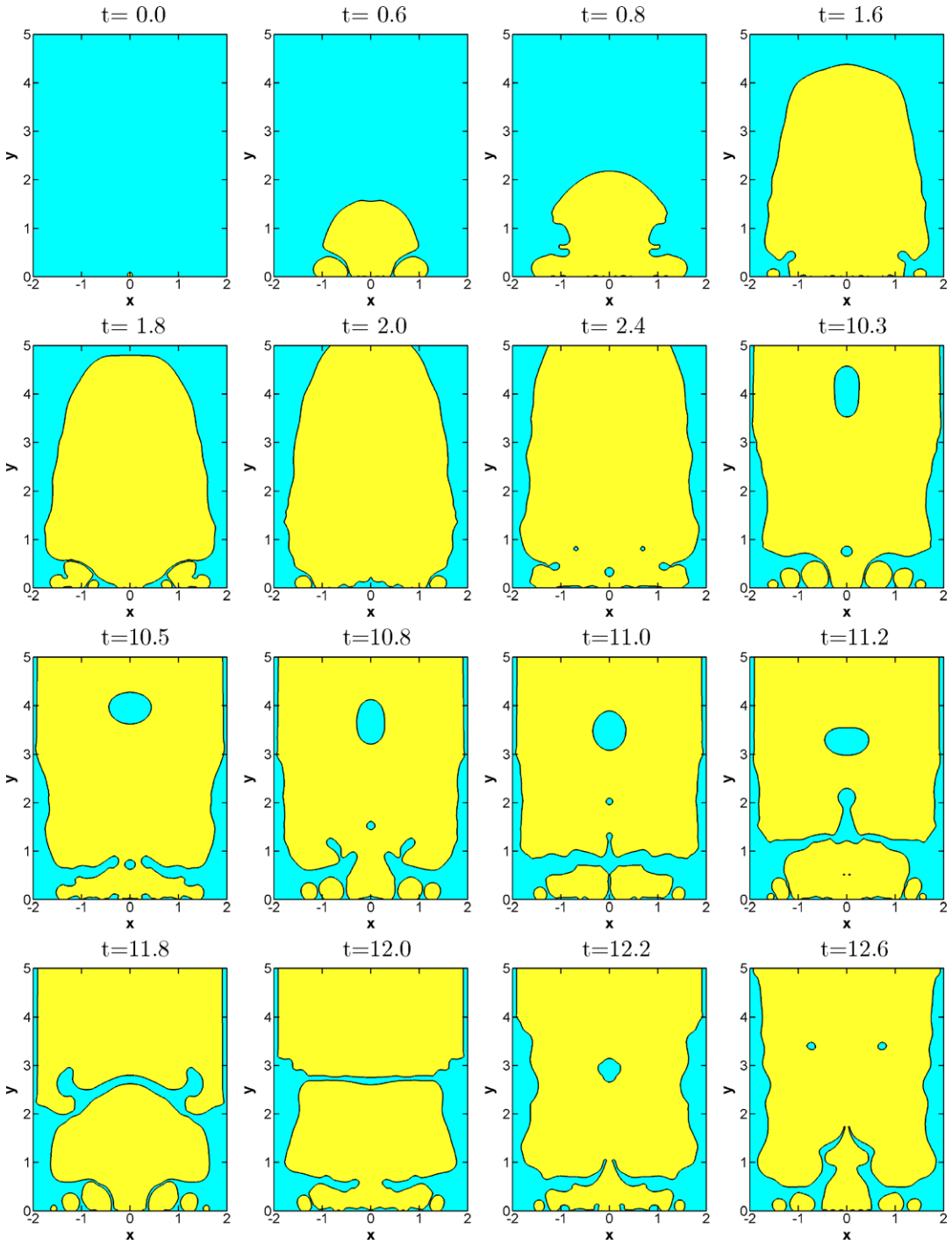

Fig. 9. Bubble growth and merger for $\Delta T = 25$ °C, $N = 17/4$, $s = 0.2$, and $\tau_w = 0.1$.

where V_v is a vapor volume computed form ϕ and V_{v0} the vapor volume that satisfies mass conservation.

The boundary conditions for the governing equations for the macro region are as follows:

at the wall,

$$u = v = 0, \quad T_l = T_w, \quad \frac{\partial \phi}{\partial y} = -\cos\varphi \tag{28}$$

at the planes of symmetry,

$$u = \frac{\partial v}{\partial x} = \frac{\partial T_l}{\partial x} = \frac{\partial \phi}{\partial x} = 0 \tag{29}$$

at the top of computational domain,

$$\frac{\partial u}{\partial y} = \frac{\partial v}{\partial y} = \frac{\partial \phi}{\partial y} = 0, \quad T_l = T_{sat} \tag{30}$$

The present numerical method was tested in our previous study [12] through the computations of bubble rise in a stationary liquid and phase-change problems including film boiling on a horizontal cylinder. The numerical results showed good agreement with the exact solutions or the empirical correlations in the literature.

3. Results and discussion

In carrying out numerical simulations of nucleate boiling, the properties of saturated water at 1 atm are used. The governing equations are non-dimensionalized by a reference length defined as $l_o = \sqrt{\sigma/g(\rho_l - \rho_v)}$ and a reference time as $t_o = \sqrt{l_o/g}$, which are evaluated as $l_o = 2.5$ mm and $t_o = 16$ ms. The contact angle is taken to be 35°, for which the data for the active site density are available in the literature. In reality, the contact angle varies dynamically between an advancing contact angle and a receding contact angle, which can be treated by the LS method as described in [21]. However, the effect of dynamic contact angle on bubble growth and heat transfer is not added in this work. The computational domain is chosen to be a region of $0 \leqslant x \leqslant 2$ and $0 \leqslant y \leqslant 50$. The side boundaries, $x = 0$ and $x = 2$, are treated as symmetric boundaries. The width of domain has little effect on the bubble dynamics and heat transfer as long as the active site density remains fixed. The height of domain is chosen to be large so that the bubble motion is not affected by the top boundary of the computational domain. To save computational time, we use non-uniform grid spacings in the y direction with the ratio of two adjacent intervals of 1.01 except near the wall, $0 \leqslant y \leqslant 0.42$, where the grid spacing is uniform as $\Delta y = h$. The grid spacing in the x direction is uniform as $\Delta x = h$. Initially the liquid temperature profile is taken to be linear in the natural convection thermal boundary layer and fluid velocity is set equal to zero. The initial thermal boundary layer thickness, δ_T, is evaluated from the correlation for the turbulent natural convective heat transfer [22] as

$$\delta_T = 7.14(\mu_l \alpha_l / \rho_l g \beta_T \Delta T)^{1/3}$$

The computations are carried out over several cycles until the effect of artificial specification of initial conditions disappears.

During computations of nucleate boiling, the distribution of active nucleation sites is specified by the number density of active sites, N, and the spacing between sites, s, as depicted in Fig. 2. The site density depends not only on wall superheat and wettability [23,24] but also on several other factors, including the procedure used in preparing the heater surface, surface finish and heater material properties, which cannot be easily quantified. As such N is treated as an external parameter in this study. For a given N, the spacing s is determined so that the primary bubble (or vapor column) forms near $x = 0$ and the bubbles do not touch the side boundary at $x = 2$. We also vary parametrically the waiting period, τ_w, between formation of two consecutive bubbles at a given site because the prediction of τ_w in most experiments with a constant heat flux condition requires a complicated calculation for simultaneously solving conduction in the solid as well as the flow and temperature field in the liquid.

To select an appropriate mesh size for computation of nucleate boiling, convergence for grid resolutions was tested with $h = 1/48$, $h = 1/96$, and $h = 1/144$. The results are plotted in Fig. 3. As the grid spacing decreases, the relative difference of the bubble growth pattern between successive mesh sizes becomes small. Although the wall heat flux is observed to vary considerably in time due to frequent bubble mergers, the value averaged over the computational period converges with reducing the grid spacing. For $h = 1/48$, $h = 1/96$, and $h = 1/144$, the area and time averaged heat fluxes are 41.3 W/cm^2, 45.0 W/cm^2, and 45.4 W/cm^2, respectively. From this results, we chose $h = 1/96$ for most of computations in this study to save the computing time without losing the accuracy of numerical results.

Fig. 4 shows the bubble growth and merger pattern for $\Delta T = 25$ °C, $N = 5/4$, $s = 0.5$, and $\tau_w = 0.1$. The locations of active sites are the same as depicted in Fig. 2b. Initially, small bubbles are sequentially placed on the heater surface

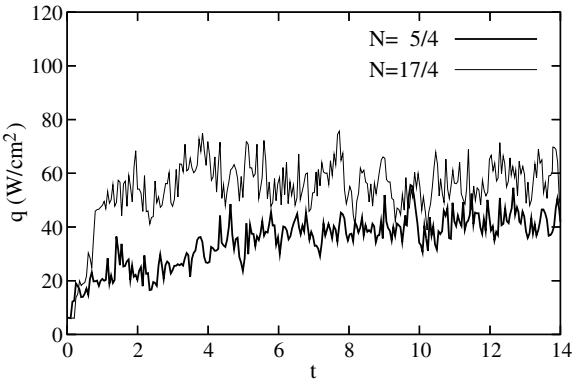

Fig. 10. Effect of number density of active sites on heat transfer for $\Delta T = 25$ °C and $\tau_w = 0.1$.

with time interval of 0.1 away from the center, $x = 0$, so that a vapor column forms near $x = 0$. Thereafter the addition of a new bubble on each cavity depends on the waiting period. In other words, if each cavity is covered with liquid during a period of τ_w, a small bubble serving as nucleus for the next cycle is placed on the cavity after the end of the waiting period. The initial bubble size chosen in the present computations is small enough to have no significant effect of the overall bubble growth. As the lateral bubble merger occurs subsequently, as shown at $t = 0.2$, a large merged bubble appears near $x = 0$. The liquid trapped by the lateral bubble merger forms a thin layer between the large merged bubble and the wall, which is referred to as a macrolayer [25]. The macrolayer is distinguished from the microlayer (or micro region), which forms just near the bubble-solid contact, as depicted in Fig. 1. The periodical

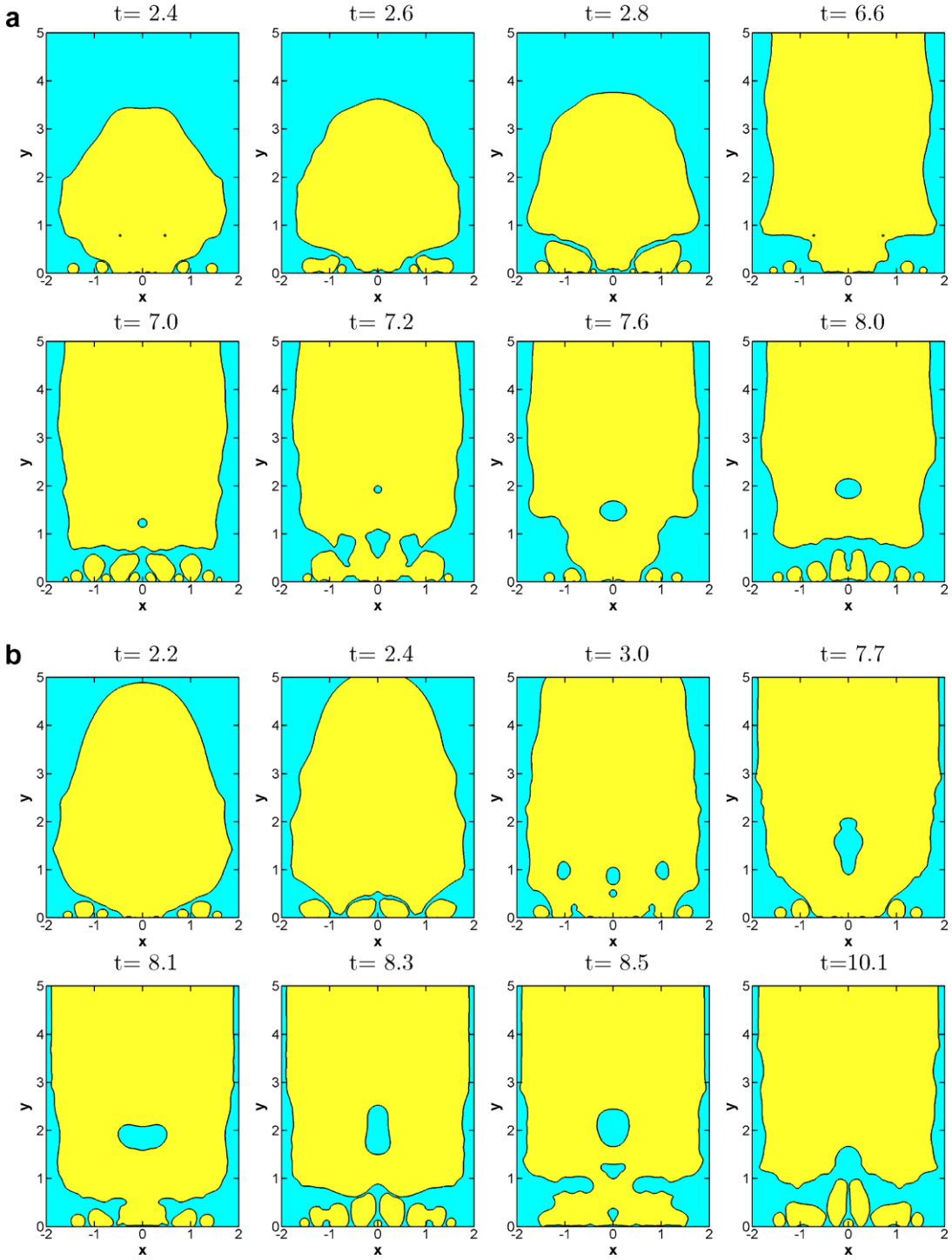

Fig. 11. Effect of wall superheat on bubble growth and merger for $N = 17/4$, $s = 0.2$, and $\tau_w = 0.1$: (a) $\Delta T = 10$ °C and (b) $\Delta T = 20$ °C.

formation of the liquid macrolayer is observed during the whole period of bubble evolution. The large bubble is fed from below by smaller bubbles (or vapor stems) as well as the vapor generation from the thin macrolayer. After several bubble mergers, the large bubble is evolved into vapor mushroom which evolves into a tall vapor column after $t = 3.2$. It is interesting to note that at $t = 9.7$ the small bubbles attached to the wall are outnumbered by the nucleation cavities. This is caused by the fact that a bubble slides away from the nucleation cavity before departing from the wall. It is also observed that small liquid droplets are entrapped into the vapor column during the bubble merger process, as seen at $3.0 \leqslant t \leqslant 3.2$ and $4.0 \leqslant t \leqslant 4.6$ as well as during later periods. Fig. 5 presents the behavior of entrapped liquid droplets with time. At $t = 4.4$, the liquid located between two merging bubbles is separated from the liquid pool and entrapped into the merged vapor column. The isolated liquid portion is developed into droplet form due to the restoring force of surface tension, as seen at $t = 5.8$. The entrapment of such a liquid droplet occurs subsequently at $t = 6.2$. The liquid droplets are eventually merged back into the liquid pool as demonstrated at $t = 6.6$.

The liquid flow field associated with the growth and merger of multiple bubbles is plotted in Fig. 6. Initially the liquid around a merged bubble attached to the wall is pushed out by the growth of bubbles. As the merged bubble grows in the vertical direction with the lateral and vertical merger of bubbles, the liquid surrounding the bubble near $x = \pm 2$ starts to flow downwards. The downward liquid motion is further developed as the merged bubble evolves into a vapor column. When the vapor column departs from the wall, a strong upward flow is also induced under the vapor column, as shown at $t = 6.4$ and $t = 12.6$.

Fig. 7 shows the temperature field around the bubbles. Initially the heat transfer required for bubble growth occurs though the superheated liquid layer surrounding the bubble including the micro region. When the merged bubble grows out of the thermal boundary layer, the heat is supplied through only the portion around the bubble base. The crowding of the isotherms underneath the merged bubble is reflective of the very high heat flux in that region. As the downward liquid flow is developed with evolution of the merged bubble, the thermal boundary becomes thinner near $x = 2$. This indicates that the forced convection induced by bubble motion is also important in nucleate boiling at high superheats. In Fig. 8, the heat transfer rates from the wall and into the vapor per unit surface area of heater are plotted. The heat fluxes are observed to vary in time, depending on the changing bubble shape with mergers occurring continuously. When the heat fluxes are averaged over the computational period ($t \geqslant 6$), except the early period when the heat transfer is affected by the initial condition, it is found that about 51% of energy from the wall is utilized in vapor production, whereas 49% goes into superheating of liquid.

When the site density is increased to $N = 17/4$, the evolution of bubble occurs as demonstrated in Fig. 9. Compared with the result for $N = 5/4$, the vapor column forms much earlier. This means that the vapor generation rate increases as the fractional area occupied by macrolayer and microlayer on the heater surface increases with the site density. Fig. 10 presents the effect of nucleation site density on the wall heat flux. When averaged over the computational period except the early period, the heat flux for

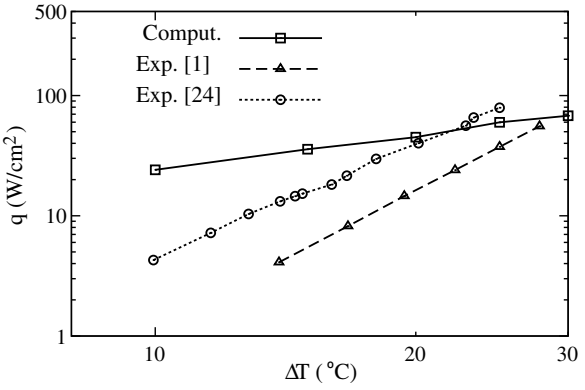

Fig. 12. Effect of wall superheat on heat transfer for $N = 17/4$, $s = 0.2$, and $\tau_w = 0.1$.

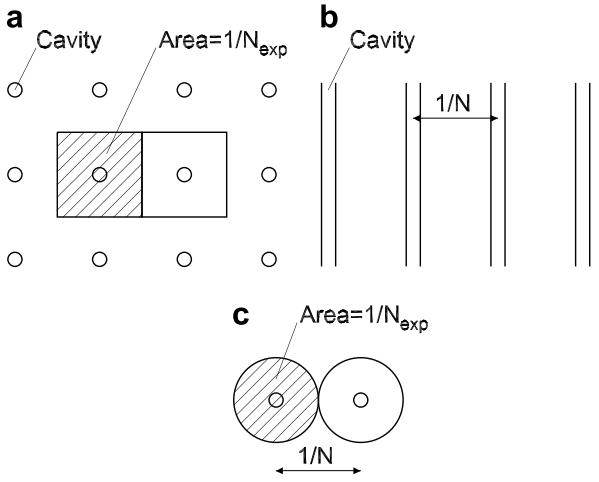

Fig. 13. Schematic for the number density of active nucleation sites: (a) N_{exp}, site density obtained experimentally, (b) N, site density used in the present two-dimensional computation, and (c) the proposed relation between N and N_{exp}.

Table 1
Data for the distribution of active nucleation sites used in the present computations

ΔT (°C)	$16N_{exp}(\#/l_o^2)$	$4N(\#/l_o)$	$s(l_o)$
10	1	0.9 → 1	–
13	4	1.8 → 2	1
15	10	2.8 → 3	1
20	80	7.9 → 8	0.4
25	350	16.6 →17	0.2

$N = 17/4$ is increased by 38% in comparison to that for $N = 5/4$.

Fig. 11 shows the effect of wall superheat on bubble growth and merger while keeping $N = 17/4$ and $\tau_w = 0.1$. With the increase in wall superheat, the formation of a vapor column occurs faster. However, the pattern of bubble growth and merger is similar for both $\Delta T = 10\ ^\circ C$ and $\Delta T = 20\ ^\circ C$. This implies that hydrodynamic transition in vapor structure observed during nucleate boiling with the increase of wall superheat will not occur if the number density of active sites and the waiting time remain constant. The dependence of time and area averaged heat flux on wall superheat is plotted in Fig. 12. The results are also compared with the experimental data obtained

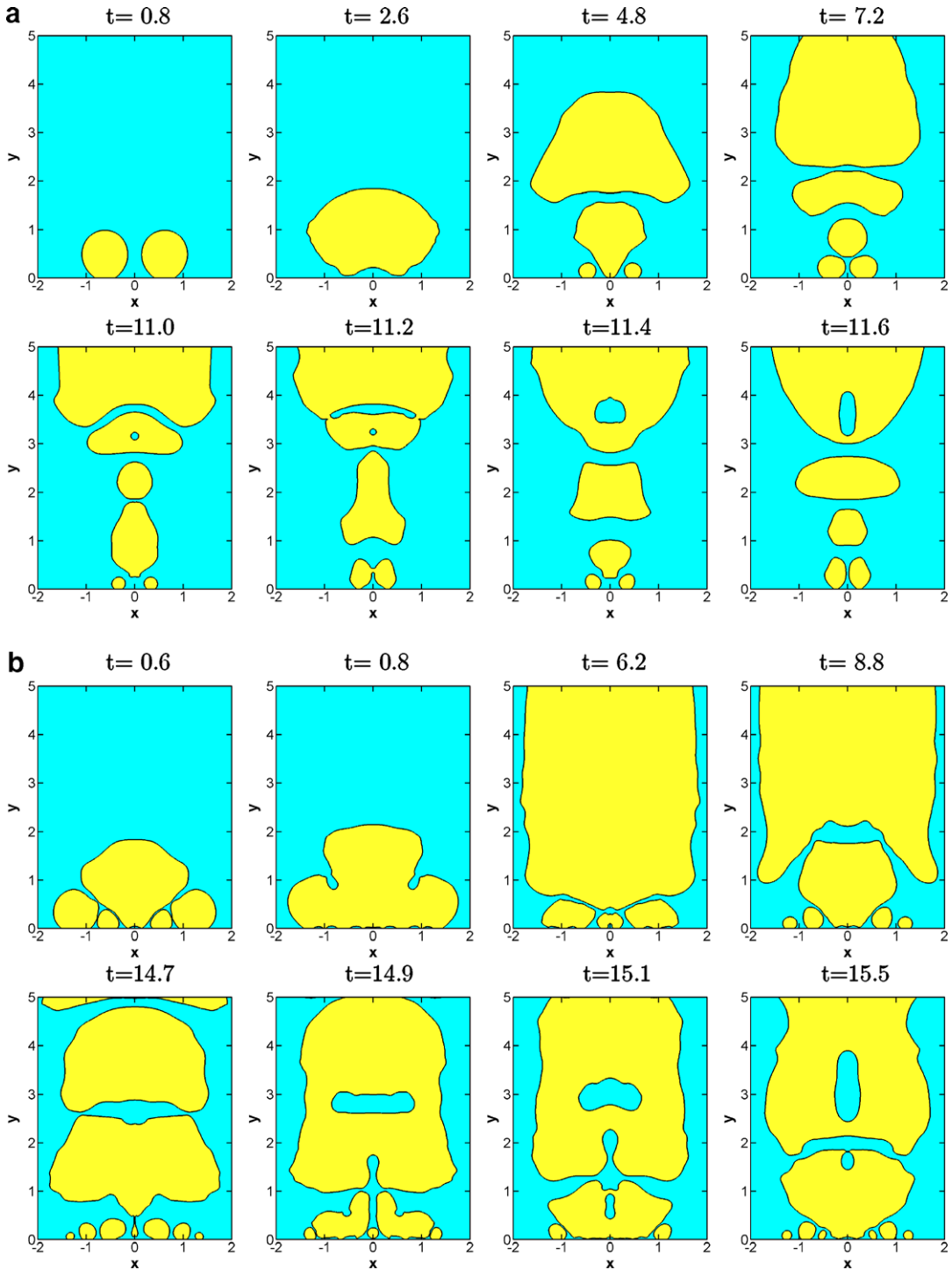

Fig. 14. Effect of wall superheat on bubble growth and merger for variable site densities and $\tau_w = 0.1$: (a) $\Delta T = 13\ ^\circ C$, $N = 2/4$, $s = 1$, and (b) $\Delta T = 20\ ^\circ C$, $N = 8/4$, $s = 0.4$.

by Gaertner [1] for nucleate boiling on a horizontal plate and by Wang and Dhir [24] for a vertical plate. The data of Gaertner were obtained on a 2/0 emery finished platinum surface whereas the data of Wang and Dhir on a copper surface with a contact angle of 35°. The orientation of the plate has little effect on boiling heat transfer for $\Delta T \geqslant 13$ °C, in which range evaporation is the dominant mode of heat transfer, as demonstrated by Nishikawa et al. [26]. Hence, the disagreement between the heat fluxes in both experiments is caused by the difference in the number density of nucleation sites. The boiling surface used by Gaertner is expected to have a very small contact angle. The heat flux obtained from the present computation varies as ΔT whereas it varies as ΔT^3 in [24] or $\Delta T^{3.75}$ in [1]. This

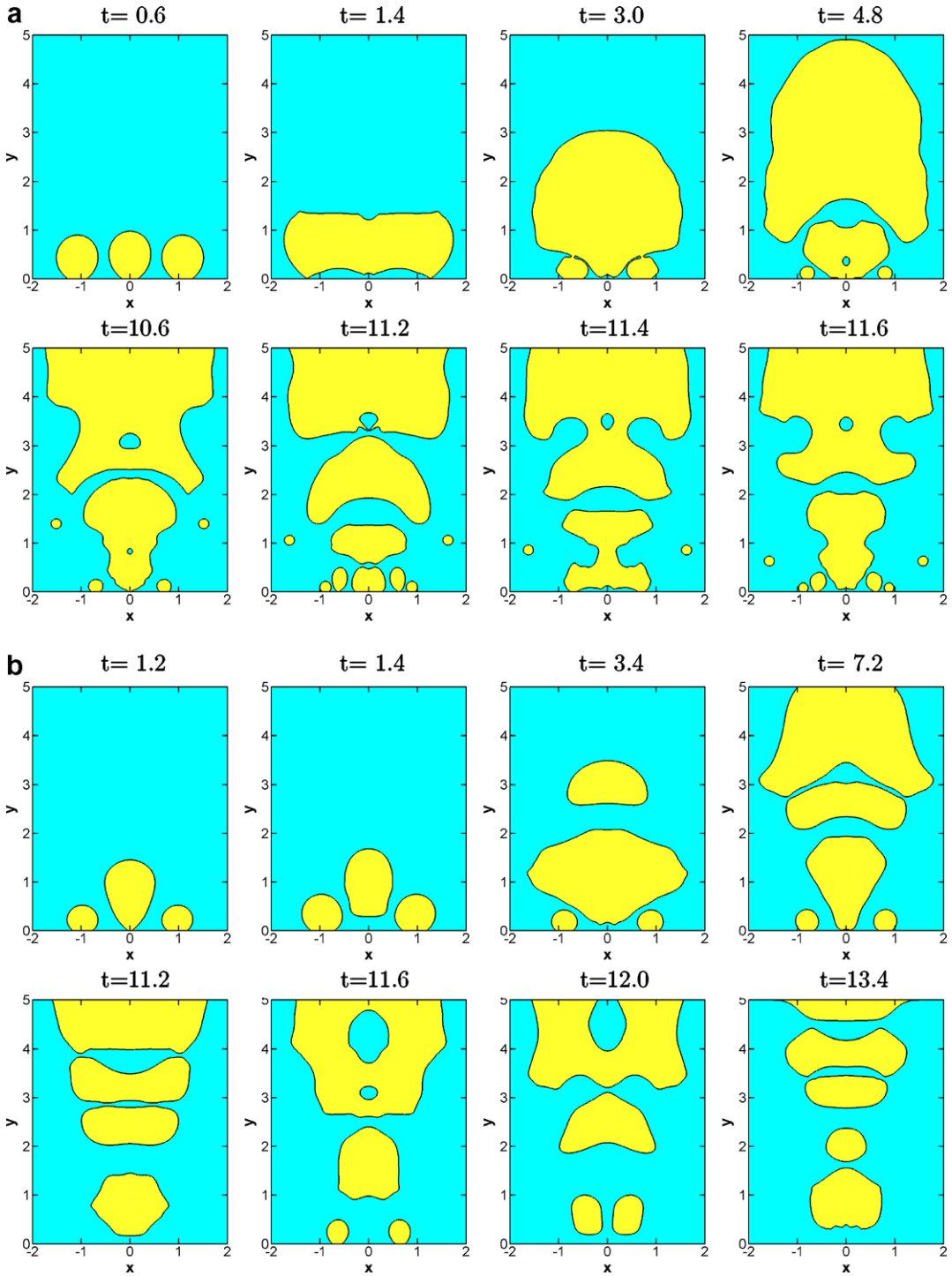

Fig. 15. Effect of waiting period on bubble growth and merger for $\Delta T = 15$ °C, $s = 1$, and $N = 3/4$: (a) $\tau_w = 0.1$ and (b) $\tau_w = 1$.

indicates that as long as nucleation site density and waiting period remain fixed, heat transfer coefficient in nucleate boiling does not change with superheat.

To simulate nucleate boiling on a real surface, we used the experimental data for the number density of active sites obtained by Wang and Dhir [24]. In the present two-dimensional computations, the site density, N, is evaluated from the experimental data, N_{exp}, which is for a two-dimensional grid. Referring to Fig. 13, we derive a relation

$$\frac{1}{N_{exp}} = \frac{\pi}{4}\left(\frac{1}{N}\right)^2 \text{ or } N = \sqrt{\frac{\pi N_{exp}}{4}} \tag{31}$$

The values of N and N_{exp} are listed in Table 1. Here, s is the spacing between sites used in the computations. Fig. 14 shows the effect of wall superheat on bubble growth and merger while the site density is also varied with the wall superheat. It is observed from Fig. 14a that at the low superheat, $\Delta T = 13$ °C, discrete bubbles are released from the heater and the bubble merger occurs occasionally. When the wall superheat is increased to $\Delta T = 20$ °C, the bubble growth pattern changes as shown in Fig. 14b. The bubble merger frequently occurs both in the vertical and horizontal directions, which leads to formation of a large vapor column and mushroom type of bubble, respectively. The large bubble is supported by vapor stems connecting the vapor mass to the heater surface. The periodic formation of macrolayer underneath the merger bubble is also observed. This transition in the bubble growth and merger pattern is consistent with the observation of Gaertner [1].

The dependence of bubble growth and merger on the waiting time, τ_w, is presented in Fig. 15. At $\tau_w = 0.1$, a vapor column is observed to form. It is noted that the small bubbles attached to the wall are outnumbered by the nucleation cavities, as shown at $t = 11.2$ and $t = 11.6$. The bubble growth pattern shift to a discrete bubble mode when τ_w is increased to 1 keeping ΔT and N constant. This indicates that the waiting period is also one of the important parameters determining the bubble growth pattern. Fig. 16 shows the variation of heat flux with wall superheat for different waiting periods. The site density, N, listed in Table 1 is used in the computations. For a given waiting period, the heat fluxes vary as $\Delta T^{3.1}$ for $\Delta T < 15$ °C, but its variation decreases to $\Delta T^{1.6}$ for the higher wall superheat. As the waiting period is reduced, the heat flux is found to increase significantly. The effect is pronounced in the high superheat range.

Several expressions for the waiting period are available in the literature [27]. However, their application, required knowledge of the cavity size or the thermal properties of a heater, as such is not so straightforward. As a practical

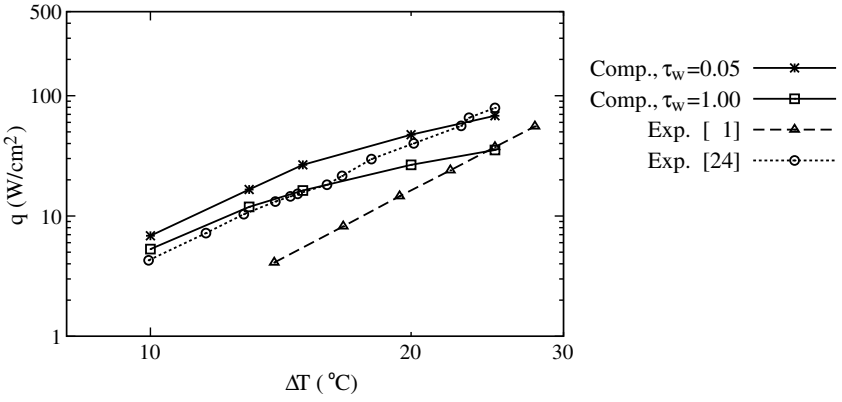

Fig. 16. Variation of heat flux with wall superheat for different waiting periods.

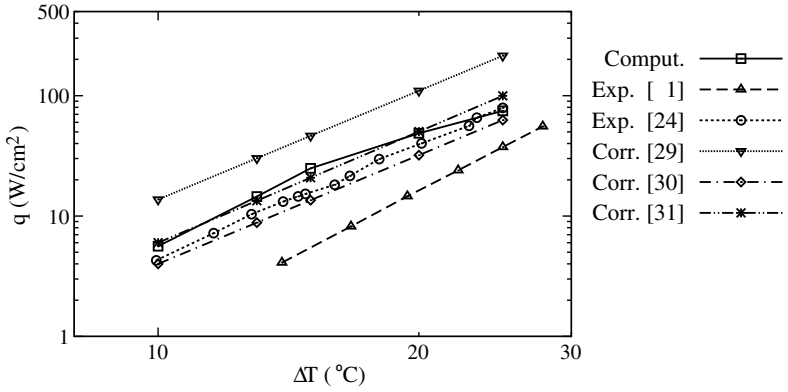

Fig. 17. Comparison of the present numerical results with experimental data and correlations.

correlation for the waiting period, the following equation was presented by Basu et al. [28] while developing a model for the wall heat flux partitioning during subcooled flow boiling:

$$\tau_w = 139.1\Delta T^{-4.1}/t_o \tag{32}$$

When using the above correlation, the heat flux as a function of wall superheat is plotted in Fig. 17. The experimental data [1,24] and three correlations available in the literature [29,30,31] are also included in Fig. 17. The correlation of Rohsenow [29] for pool nucleate boiling is expressed as

$$q = \mu_l h_{lv}\sqrt{\frac{g(\rho_l-\rho_v)}{\sigma}}\left(\frac{c_l\Delta T}{C_s h_{lv}}\right)^3 Pr_l^{-3} \tag{33}$$

where C_s depends on heater material and fluid combination and its value is 0.013 for water–copper combination. As shown by Liaw and Dhir [30], C_s can be quantified as a function of contact angle. Its value is 0.02 for a contact angle of 35°. A more comprehensive correlation of Stephan and Abdelsalam [31], which was obtained form nearly 5000 existing experimental data for nucleate boiling on horizontal surfaces, is expressed as

$$\frac{qD_d}{k_l\Delta T} = 0.23\left(\frac{qD_d}{k_l T_{sat}}\right)^{0.674}\left(\frac{\rho_v}{\rho_l}\right)^{0.297}\left(\frac{h_{lv}D_d^2}{\alpha_l^2}\right)^{0.371}\left(\frac{\rho_l-\rho_v}{\rho_l}\right)^{-1.73}\left(\frac{\rho_l\alpha_l^2}{\sigma D_d}\right)^{0.35} \tag{34}$$

where D_d is the bubble diameter at departure, $D_d = 0.0208\varphi\sqrt{\sigma/g(\rho_l-\rho_v)}$. It is observed from Fig. 17 that the heat fluxes obtained from the present work are comparable to the experimental data with the corresponding active site density [24] and are within at most ±25% deviation with those predicted from Stephan and Abdelsalam's correlation. Also, the dependence of the computed

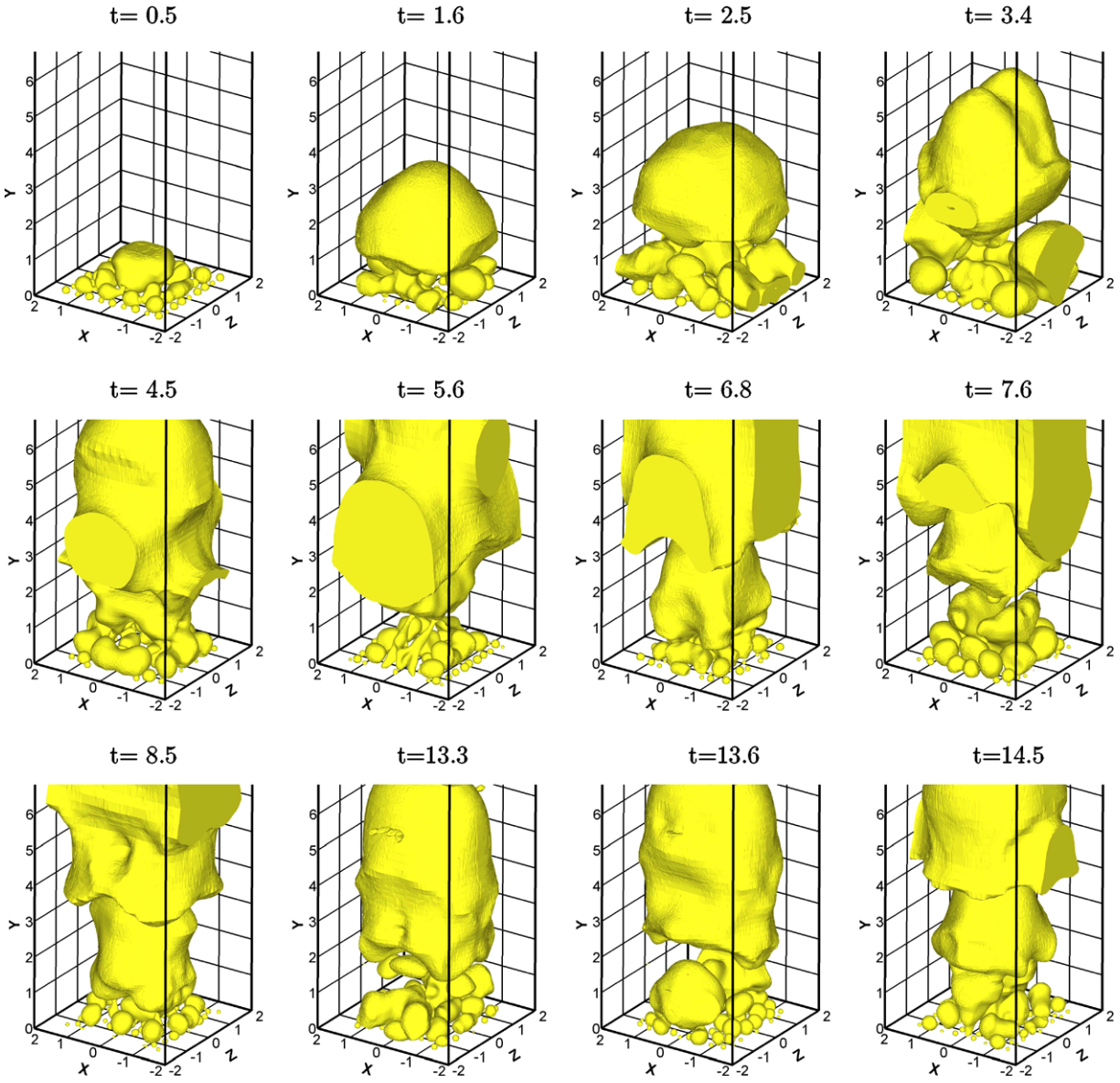

Fig. 18. Bubble growth and merger obtained from three-dimensional computation for $\Delta T = 20$ °C, $N_{exp} = 81/16$, $s = 0.35$, and $\tau_w = 0.1$.

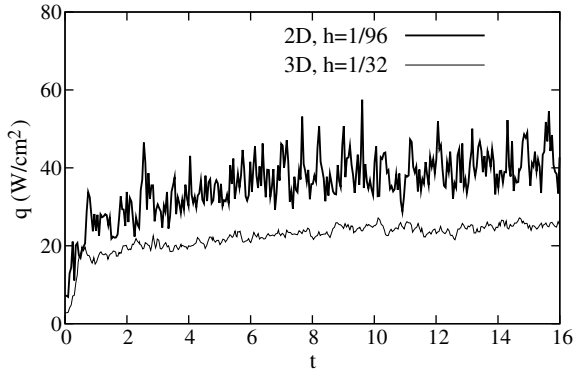

Fig. 19. Wall heat fluxes obtained from two- and three-dimensional computations for $\Delta T = 20$ °C and $\tau_w = 0.1$.

heat flux on wall superheat is consistent with the experimental data and the three correlations except near $\Delta T = 25$ °C, where the variation of the computed heat flux on wall superheat becomes weaker.

A three-dimensional (3D) simulation of nucleate boiling is performed on the domain, $0 \leqslant x \leqslant 2$, $0 \leqslant y \leqslant 20$ and $0 \leqslant z \leqslant 2$. The grid spacing is chosen as $h = 1/32$, which is much coarser than $h = 1/96$ used for two-dimensional (2D) computations. The 3D evolution of bubble is demonstrated in Fig. 18. The bubble growth and merger pattern, including frequent bubble mergers in the vertical and lateral directions and the formation of a large vapor column or mushroom type bubble, is qualitatively comparable to the 2D results plotted in Fig. 14b. However, the formation of macrolayer underneath the merger bubble is not captured clearly in the 3D computation using a coarse grid. Fig. 19 shows the wall heat fluxes obtained from 2D and 3D computations. In comparison to the 2D case, the time and area averaged heat flux obtained from the 3D computation is lower by about 39%. This is mainly caused by the use of a coarser grid which fails to capture the macrolayer underneath the merged vapor bubble. The three-dimensional simulation on a finer grid with $h = 1/96$, which requires a tremendous computational time and hence efficient numerical techniques such as parallel computing, will be undertaken in the future.

4. Conclusions

1. Numerical simulations of bubble dynamics and heat transfer in nucleate boiling at high wall superheats have been performed successfully.
2. Based on the numerical simulations, it is shown that in nucleate boiling at low wall superheats discrete vapor bubbles are released from the heater and the bubble merger occurs occasionally. With the increase in wall superheat, the bubble merger frequently occurs both in the vertical and horizontal directions, which leads to formation of a large vapor column or mushroom type bubbles. This transition in the bubble growth and release pattern is consistent with visual observations reported in the literature.
3. In nucleate boiling, the steep variation of heat flux with wall superheat is caused not only by the increase in the number density of active sites with wall superheat but also by the reduction in the waiting period.
4. The heat fluxes obtained from the present 2D analysis are within ±25% with those predicted from Stephan and Abdelsalam's correlation.
5. In this work, 2D computations are used as the computational time for 3D case is excessively large. A sample 3D calculations with a coarser grid gives heat flux that is about 40% lower than that for corresponding 2D case.

Acknowledgement

This work received support from NASA Microgravity Fluid Physics program.

References

[1] R.F. Gaertner, Photographic study of nucleate pool boiling on a horizontal surface, J. Heat Transfer 87 (1965) 17–29.
[2] V.K. Dhir, Boiling Heat Transfer, Annu. Rev. Fluid Mech. 30 (1998) 365–401.
[3] V.K. Dhir, Mechanistic prediction of nucleate boiling heat transfer-achievable or a hopeless task? J. Heat Transfer 128 (2006) 1–12.
[4] R.C. Lee, J.E. Nydahl, Numerical calculation of bubble growth in nucleate boiling from inception through departure, J. Heat Transfer 111 (1989) 474–479.
[5] S.W.J. Welch, Direct simulation of vapor bubble growth, Int. J. Heat Mass Transfer 41 (1998) 1655–1666.
[6] G. Son, V.K. Dhir, N. Ramanujapu, Dynamics and heat transfer associated with a single bubble during nucleate boiling on a horizontal surface, J. Heat Transfer 121 (1999) 623–631.
[7] G. Son, N. Ramanujapu, V.K. Dhir, Numerical simulation of bubble merger process on a single nucleation site during pool nucleate boiling, J. Heat Transfer 124 (2002) 51–62.
[8] A. Mukherjee, V.K. Dhir, Study of lateral merger of vapor bubbles during nucleate pool boiling, J. Heat Transfer 126 (2004) 1023–1039.
[9] S. Shin, S.I. Abdel-Khalik, D. Juric, Direct three-dimensional numerical simulation of nucleate boiling using the level contour reconstruction method, Int. J. Multiphase Flow 31 (2005) 1231–1242.
[10] P.C. Wayner Jr., Evaporation and stress in the contact line region, in: V.K. Dhir, A.E. Bergles (Eds.), Proceedings of The Engineering Foundation Conference on Pool and External Flow Boiling, Santa Barbara, California, 1992, pp. 251–256.
[11] J.H. Lay, V.K. Dhir, Shape of a vapor stem during nucleate boiling of saturated liquids, J. Heat Transfer 117 (1995) 394–401.
[12] G. Son, V.K. Dhir, A level set method for analysis of film boiling on an immersed solid surface, Numer. Heat Transfer, Part B 52 (2007) 153–177.
[13] D.Q. Nguyen, R.P. Fedkiw, M. Kang, A boundary condition capturing method for incompressible flame discontinuities, J. Comput. Phys. 172 (2001) 71–98.
[14] R.P. Fedkiw, T. Aslam, B. Merriman, S. Osher, A non-oscillatory Eulerian approach to interfaces in multimaterial flows (the ghost fluid method), J. Comput. Phys. 152 (1999) 457–492.
[15] F. Gibou, R.P. Fedkiw, L.-T. Cheng, M. Kang, A second-order-accurate symmetric discretization of the Poisson equation on irregular domains, J. Comput. Phys. 176 (2002) 205–227.

[16] S. Marella, S. Krishnan, H. Liu, H.S. Udaykumar, Sharp interface Cartesian grid method I: an easily implemented technique for 3D moving boundary computations, J. Comput. Phys. 210 (2005) 1–31.
[17] X.-Y. Luo, M.-J. Ni, A. Ying, M.A. Abdou, Level set method for multiphase incompressible flow with phase change, Numer. Heat Transfer, Part B 48 (2005) 425–444.
[18] F. Gibou, L. Chen, D. Nguyen, S. Banerjee, A level set based sharp interface method for the multiphase incompressible Navier–Stokes equations with phase change, J. Comput. Phys. 222 (2007) 536–555.
[19] M. Sussman, K.M. Smith, M.Y. Hussaini, M. Ohta, R. Zhi-Wei, A sharp interface method for incompressible two-phase flows, J. Comput. Phys. 221 (2007) 469–505.
[20] G. Son, A level set method for two-fluid flows with immersed solid boundaries, Numer. Heat Transfer, Part B 47 (2005) 473–489.
[21] G. Son, N. Hur, A level set formulation for incompressible two-phase flows on non-orthogonal grids, Numer. Heat Transfer, Part B 48 (2005) 303–316.
[22] W.M. Kays, M.E. Crawford, Convective Heat and Mass Transfer, McGraw-Hill Book Company, New York, 1980, pp. 328.
[23] G. Kocamustafaogullari, M. Ishii, Interfacial area and nucleation site density in boiling systems, Int. J. Heat Mass Transfer 26 (1983) 1377–1387.
[24] C.H. Wang, V.K. Dhir, Effect of surface wettability on active nucleation site density during pool boiling of saturated water, J. Heat Transfer 115 (1993) 659–669.
[25] Y. He, M. Shoji, S. Maruyama, Numerical study of high heat flux pool boiling heat transfer, Int. J. Heat Mass Transfer 44 (2001) 2357–2373.
[26] K. Nishikawa, Y. Fujita, H. Ohta, Effect of surface configuration on nucleate boiling heat transfer, Int. J. Heat Mass Transfer 27 (1974) 1559–1571.
[27] Y.-Y. Hsu, R.W. Graham, Transport Processes in Boiling and Two-phase Systems, American Nuclear Society, Lagrange Park, Illinois, 1986, pp. 15–18.
[28] N. Basu, G.R. Warrier, V.K. Dhir, Wall heat flux partitioning during subcooled flow boiling: part 1. model development, J. Heat Transfer 127 (2005) 131–140.
[29] W.M. Rohsenow, A method of correlating heat transfer data for surface boiling of liquids, J. Heat Transfer 74 (1952) 969–976.
[30] S.P. Liaw, V.K. Dhir, Void fraction measurement during saturated pool boiling of water on partially wetted vertical surfaces, J. Heat Transfer 111 (1989) 731–783.
[31] K. Stephan, M. Abdelsalam, Heat transfer correlation for natural convection boiling, Int. J. Heat Mass Transfer 23 (1980) 73–87.